Volkova N. E., Khvostova L. V., Galaida A. P., Gavrilova L. Ya., Cherepanov V. A.
Chimica Techno Acta. 2018. Vol. 5, No. 1. P. 55–79.
ISSN 2409–5613

DOI: 10.15826/chimtech.2018.5.1.04

N. E. Volkova, L. V. Khvostova, A. P. Galaida, L. Ya. Gavrilova, V. A. Cherepanov

Department of Physical and Inorganic Chemistry, Ural Federal University, 19 Mira St., Ekaterinburg, 620002, Russian Federation
nadezhda.volkova@urfu.ru

Phase equilibria, crystal structure and oxygen nonstoichiometry of the complex oxides in Sm – (Sr, Ba) – (Co, Fe) – O systems

Present paper contains available information on the phase equilibria in the Sm – (Sr, Ba) – (Co, Fe) – O systems, including the synthesis routes used, crystal structure, which is often depended on oxygen nonstoichiometry, the data on thermodynamic stability of complex oxides, the obtained results on the homogeneity ranges of solid solutions, formed in the systems, and graphical presentation of phase relations in a form of phase diagrams.

Keywords: phase equilibrium; solid solutions; crystal structure; phase diagram

Received: 18.01.2018. Accepted: 14.02.2018. Published: 10.05.2018.

Introduction

Complex oxides based on samarium, alkali earth (Sr, Ba) and 3d transition (Co, Fe) metals have attracted great interest of researchers during the last few decades because of a variety of potential practical applications such as cathodes for the SOFCs [1–6], membranes [7–9], magnets [10–12], catalysts [13–16], gas sensors [17–19]. Traditionally, most of the publications devoted to the modern materials focus on their functional properties. At the same time, information concerning the phase equilibria and stability ranges often remains undisclosed or appears fragmentary. Systematic studies of phase equilibria are rare. Another important characteristic of these oxides, closely linked with their stability, is the value of oxygen nonstoichiometry.

Since the overall information concerning the crystal structure, phase equilibria, phase stability, oxygen nonstoichiometry and defect structure constitutes the physicochemical basis of the preparation and usage of these materials, it is vitally important. Thus, the present work was aimed to overview the available data concerning the phase equilibria within the Sm – (Sr, Ba) – (Co, Fe) – O system, as well as the crystal structure and oxygen nonstoichiometry of the complex oxides formed in these systems.

Phase equilibria in Sm – Co – O system

A systematic study of phase equilibria in the Sm – Co – O system was performed for the first time by Kropanev et al [20, 21], and later by Kitayama [22]. Samarium

cobaltate $SmCoO_3$ was the only phase found to exist in this system. This complex oxide was first described by Wold and Ward [23] as perovskite type with the cubic structure (a = 3.75±0.01 Å), although later it was suggested that the ideal perovskite structure is orthorhombically distorted (Table 1) [22, 24–28].

Different techniques have been used for preparation of $SmCoO_3$: a conventional ceramic technique from oxides [20, 21], or from mixture of nitrates dried from their solution [24, 27], or from the mixture of cobalt carbonate and samarium nitrate [23]; via co-precipitation from the nitrates solution by Na_2CO_3 with following annealing in air [22]. The mechanism and kinetics of solid state $SmCoO_3$ synthesis from oxides has been studied in [29–32]. It was shown that the diffusion stage of synthesis occur by transport of Co^{n+} (n = 2, 3) and O^{2-} ions through the layer of product to the reaction zone that is located on the $SmCoO_3$ – Sm_2O_3 interphase boundary [29, 30]. The kinetics of synthesis depends on the grain size, oxygen partial pressure and compacting pressure of oxides mixture for both Sm_2O_3 – CoO and Sm_2O_3 – Co_3O_4 systems [30, 31].

Samarium cobaltate $SmCoO_3$ is stable in air up to the incongruent melting point equal to 1344±4 °C [21]. The subsolidus part of the "T – composition" phase diagram for the Sm – Co – O system in air is shown in Fig. 1.

Thermodynamic properties and stability ranges measured by means of EMF technique in the galvanic cells with solid electrolyte are presented in [20, 21, 33, 34] and those measured by thermogravimetric (TGA) method – in [22]. The equilibrium oxygen partial pressure for the reaction:

$$\frac{1}{2}\,Sm_2O_3 + CoO + \frac{1}{4}\,O_2 = SmCoO_3, \quad (1)$$

examined in the galvanic cell with the solid electrolyte (ZrO_2 doped by Y_2O_3) can be written as follows [20]:

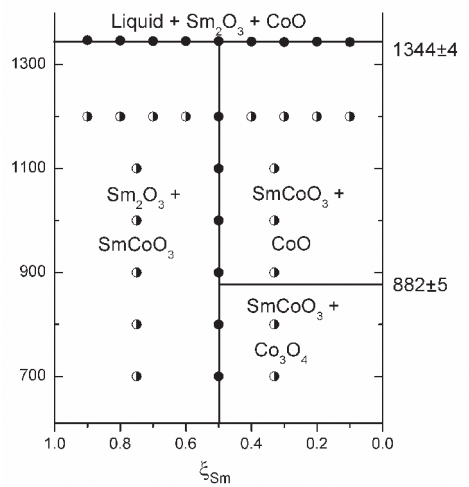

Fig. 1. The cross-sections of phase diagram for the Sm – Co – O system "T – composition" in air [21]

Table 1

The values of unit cell parameter of orthorhombically distorted $SmCoO_3$ (*Pbnm* space group)

a, Å	*b*, Å	*c*, Å	Treatment conditions	Ref.
5.284±0.006	5.343±0.006	7.506±0.006	Prepared in air, with the excess of CoO	[22]
5.283±0.005	5.344±0.005	7.502±0.005	Prepared in air, with the excess of Sm_2O_3	[22]
5.289	5.354	7.541	Treated in oxygen at 930 °C	[24,25]
5.294±0.002	5.352±0.002	7.504±0.003	Prepared at 930 °C and under pressure 60 kbar	[26,27]
5.2831(1)	5.3502(1)	7.4962(1)	Standard solid state ceramic procedures at 1200 °C in air, with intermediate grindings	[28]

$$\lg\left(\frac{P_{O_2}}{P^{\circ}_{O_2}}\right) = -\frac{14800}{T, K} + 8.46,$$

$$(1076 \le T, \text{K} \le 1474). \quad (2)$$

where is a standard pressure, and standard Gibbs energy corresponding to the reaction (1) is expressed by the equations:

Ref. [33]:

$$\Delta G^{\circ}_1(J/mol) = -70820 + 40.47 \times T(K), \quad (3)$$

$$(1076 \le T, \text{K} \le 1474).$$

Ref. [34]:

$$\Delta G^{\circ}_1(J/mol) = -52530 + 25.0 \times T(K), \quad (4)$$

$$(1080 \le T, \text{K} \le 1180).$$

The standard Gibbs energy of formation from elements $\Delta G^{\circ}_f(SmCoO_3)$ was presented in [33] by following equation:

$$\Delta G^{\circ}_f(J/mol) = \\ = -1215600 - 3.66 \times T \times \lg T + 270.5. \quad (5)$$

The cross sections of phase diagram for the Sm – Co – O system corresponding to the different fixed parameters are shown in Figs. 2–4.

Phase equilibrium in Sm – Fe – O system

The detailed study of phase equilibria in the Sm – Fe – O system was performed by Kitayama and Katsura (Fig. 5) [35] and later by Parida et al [36]. Two ternary oxides – $SmFeO_{3-\delta}$ and $Sm_3Fe_5O_{12}$ – exist in the system. Samarium ferrite $SmFeO_{3-\delta}$ possesses orthorhombically distorted perovskite structure (space group *Pbnm*) [24, 35–41], $Sm_3Fe_5O_{12}$ crystallizes in the cubic garnet structure (space group *Ia3d*) [35, 36, 42–45].

It was shown that despite of Sm_2O_3/Fe_2O_3 ratio $SmFeO_{3-\delta}$ always appears as the first product in the initial stages of synthesis within the temperature range 700–1300 °C; the reaction rate was greater in the mixtures with the iron oxide excess [46]. This is consistent with the fact that most of the samples with the nominal

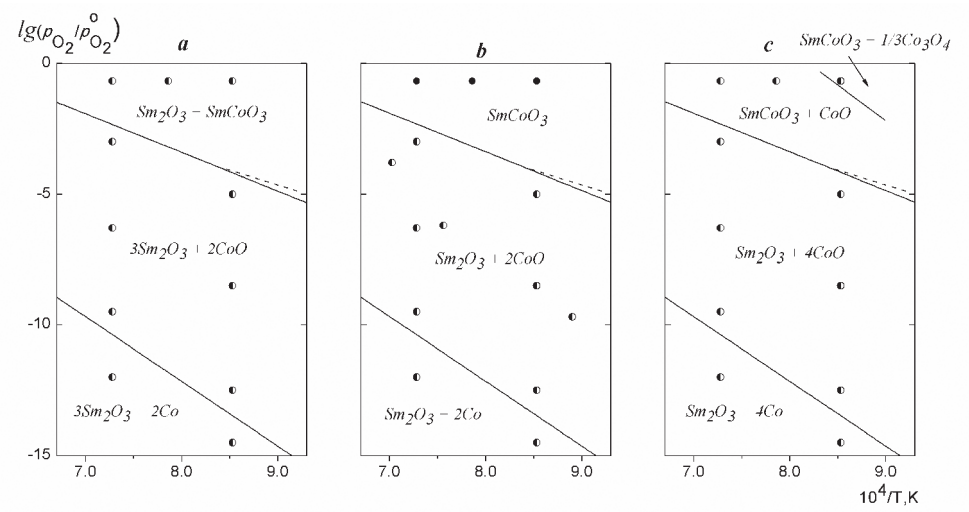

Fig. 2. The cross sections of phase diagram for the Sm – Co – O system at fixed metal ratio (ε_{Sm}): *a* – 0.75; *b* – 0.5 and ***c*** – 0.33. Filled circles – single-phase, half-filled circles – double-phase samples [20]. Dashed lines are $SmCoO_3$ decomposition oxygen partial pressure calculated from [34]

composition of $Sm_3Fe_5O_{12}$ fired at 700 °C contained $SmFeO_{3-\delta}$ as the impurity phase, even if the citrate technique had been used as preparation method [43]. Taking into account these findings, the temperature of final synthesis' anneals in order to get a single phase samarium ferrite with garnet structure has to be high enough (≥ 1200 °C). The unit cell parameters for the samarium ferrites $SmFeO_{3-\delta}$ and $Sm_3Fe_5O_{12}$ are listed in Table 2.

A detailed study of crystal structure performed on the single crystal of $Sm_3Fe_5O_{12}$ within the range $20 \le T$, K ≤ 297 reveals the second order phase transition at 68 and 40 K [44]. The coefficients for the temperature dependency of unit cell parameter for $Sm_3Fe_5O_{12}$

$$a(T) = a_0 + a_1 + a_2 T^2 \qquad (6)$$

are listed in Table 3.

Thermodynamic properties of samarium ferrites were reported in [35, 36, 47–49]. At 1200 °C $SmFeO_{3-\delta}$ is stable from air down to $pO_2 = 10^{-12.68}$ atm and $Sm_3Fe_5O_{12}$ – down to $pO_2 = 10^{-3.72}$ atm [35].

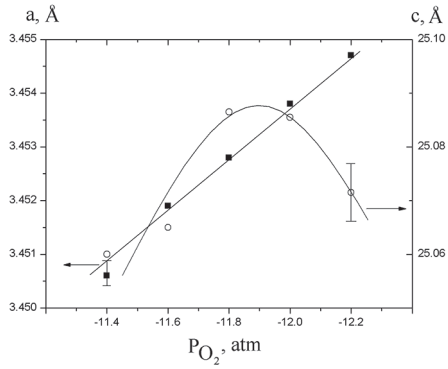

Fig. 4. Gibbs triangle of phase equilibria in the Sm – Co – O system at 1273 K [20]. The values of equilibrium oxygen pressure in logarithmic scale are: 1) ≈ 5, 2) ≈1.3, 3) –3.17, 4) –11.8

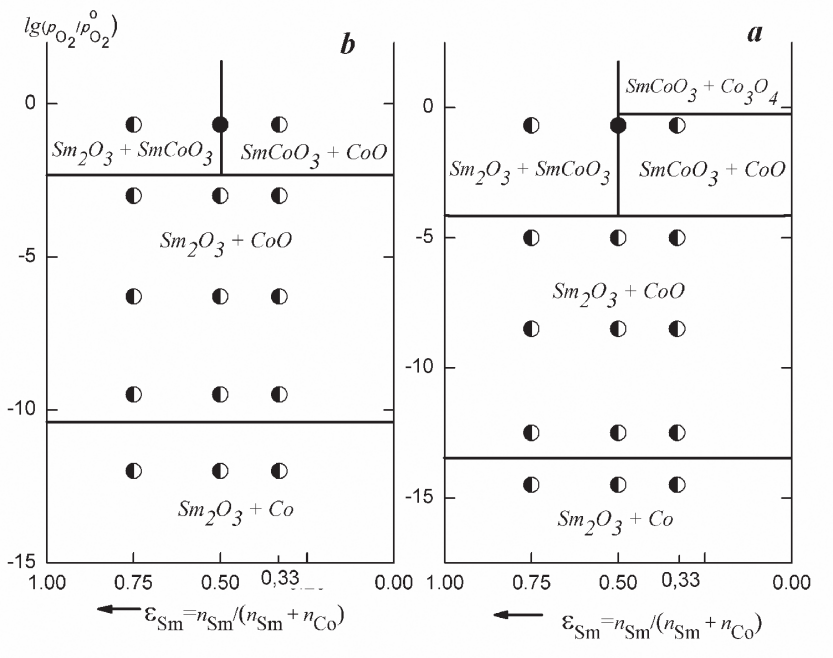

Fig. 3. The cross sections of phase diagram for the Sm – Co – O system at fixed temperatures: *a* – 1173 K; *b* – 1373 K [20]. The composition is represented by molar fraction of metal components

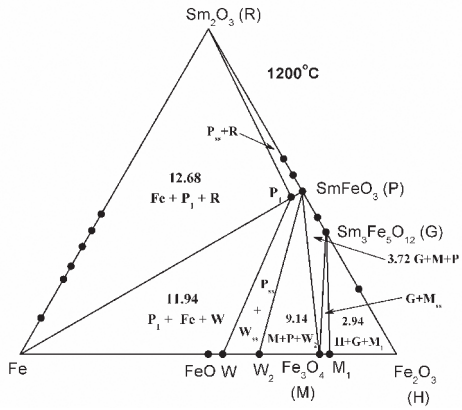

Fig. 5. Phase equilibria in the Fe – Fe_2O_3 – Sm_2O_3 system at 1200 °C (mol%) [35]. Numbers in the figure mean values of –log pO_2 at which three crystalline phases are in equilibrium state. Letters R, P, G, and M represent stoichiometric compositions of Sm_2O_3, $SmFeO_3$, $Sm_3Fe_5O_{12}$, and Fe_3O_4, respectively. M_1 is the end member of the magnetite solid solution with chemical composition $Fe_{2.957}O_4$. P_{ss}, W_{ss}, and M_{ss} are the solid solutions of $SmFeO_3$ from P to P_1, of FeO from W to W_2, and Fe_3O_4 from M to M_1, respectively. W and W_2 are the end members of the wustite solid solution with chemical compositions $FeO_{1.049}$ and $FeO_{1.166}$, respectively. P_1 is nonstoichiometric perovskite phase $SmFeO_{2.982}$

Table 2

The values of unit cell parameter of $SmFeO_{3-\delta}$ and $Sm_3Fe_5O_{12}$

$SmFeO_{3-\delta}$					$Sm_3Fe_5O_{12}$	
(3 – δ)	*a*, Å	*b*, Å	*c*, Å	Ref.	*a*, Å	Ref.
–	5.394	5.592	7.711	[24, 37]	12.519±0.002	[35]
3.0	5.398±0.002	5.598±0.002	7.708±0.002	[35]	12.529±0.001	[42]
2.982	5.398±0.001	5.591±0.001	7.706±0.001	[35]	–	–
–	5.400±0.001	5.597±0.001	7.711±0.001	[38]	–	–
–	5.39853(4)	5.59683(4)	7.70715(5)	[39]	–	–
3.034	5.588(3)*	7.710(6)*	5.392(3)*	[40]	–	–
–	5.39	5.58	7.71	[41]	–	–

* *Pnma* space group

Table 3

Polynomial's coefficients (Eq. 6) for the single crystal $Sm_3Fe_5O_{12}$ unit cell parameter [44]

Temperature range (K)	a_0 (Å)	$a_1\times10^4$ (Å/K)	$a_0\times10^6$ (Å/K²)
20–297	12.5235	-1.53×10^{-1}	2.21×10^{-1}
20–40	12.5197	2.24	–3.18
40–68	12.5270	–1.407	1.35
68–297	12.5226	-4.9×10^{-2}	1.95×10^{-1}

The limits of thermodynamic stability for $SmFeO_{3-\delta}$ and $Sm_3Fe_5O_{12}$ that can be represented by the reactions (7) and (8) [36] are shown in Fig. 6.

$$18\ SmFeO_3 + 4\ Fe_3O_4 + O_2 = 6\ Sm_3Fe_5O_{12} \quad (7)$$

$$\tfrac{2}{3}\ Sm_2O_3 + \tfrac{4}{3}\ Fe + O_2 = SmFeO_3 \quad (8)$$

The temperature dependencies of Gibbs energy that correspond to the processes (7) and (8) are written as follows [36]:

$$\Delta\mu(O_2)/kJ\times mol^{-1}\ (\pm 0.8) = -607.3 + 0.2333\times(T/K)$$
$$1030 \le T/K \le 1252 \quad (9)$$

$$\Delta\mu(O_2)/kJ\times mol^{-1}\ (\pm 0.6) = -590.7 + 0.1587\times(T/K)$$
$$1005 \le T/K \le 1259 \quad (10)$$

The phase diagram for the Sm – Fe – O system in the "$\log(pO_2)$ – composition" coordinates at 1250 K is shown in Fig 7.

The heat capacity anomaly that was detected for $SmFeO_3$ at 673 K and for $Sm_3Fe_5O_{12}$ at 560 K was attributed to the second-order magnetic order ↔ disorder transformation [36].

Phase equilibrium in Sm – Sr – Co – O system

Two types of solid solutions were found to exist in the Sm – Sr – Co – O system: with the perovskite structure and with the K_2NiF_4 type structure.

The perovskite-type solid solutions $Sm_{1-x}Sr_xCoO_{3-\delta}$ can be prepared by the conventional ceramic technique [1, 50–52] or through the solution precursors methods [53–59] within the temperature range 900–1200 °C in air or in the oxygen flow. It should be noted that using of conventional ceramic technique often yields the samples contaminated by small amounts of impurities, for example, they were detected in the $Sm_{0.5}Sr_{0.5}CoO_{3-\delta}$ sample after annealing at 1100 °C in air for 240 h. On the contrary, using the solution precursors routes allow to obtain single-phase samples much faster.

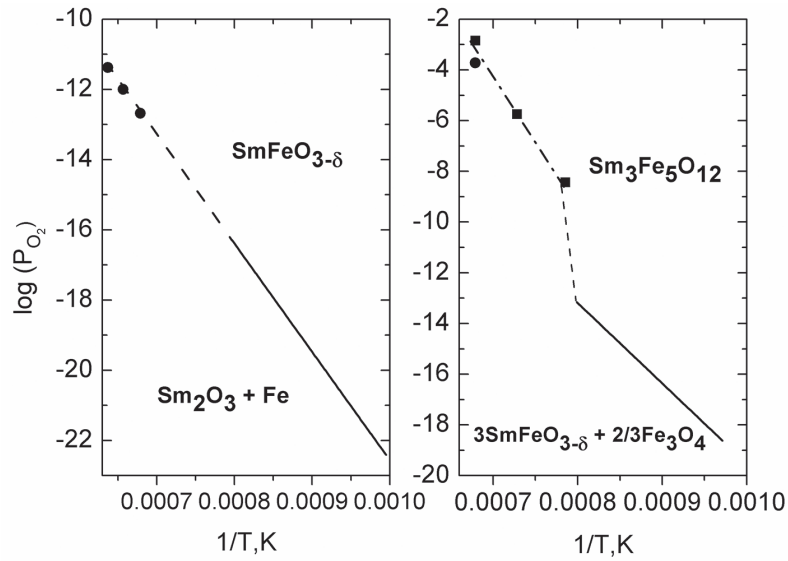

Fig.6. Thermodynamic stability of the $SmFeO_3$ and $Sm_3Fe_5O_{12}$, constructed from the data in [36] (straight line); circle points are taken from [47], square points are calculated from [48, 49]

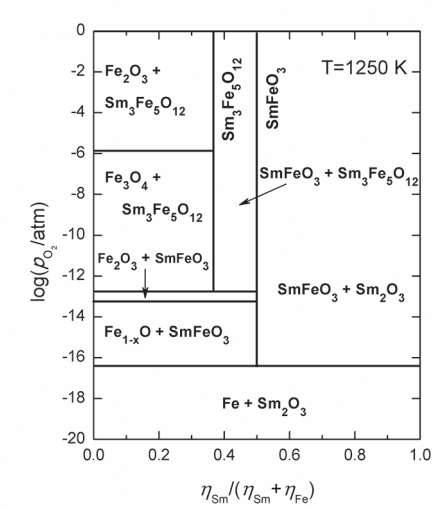

Fig. 7. The phase diagram for the Sm – Fe – O system at 1250 K [36]

The synthesis conditions, structure type and unit cell parameters for the various $Sm_{1-x}Sr_xCoO_{3-\delta}$ compositions are listed in Table 4.

Sm-enriched $Sm_{1-x}Sr_xCoO_{3-\delta}$ ($0 < x < 0.5$) obtained at 1200 °C in air possesses the perovskite structure with orthorhombic [1, 52] or tetragonal [53] distortions. The increase of strontium content leads to the decrease of orthorhombic distortions [1]. It should be noted that annealing temperature not less than 1200 °C is important since the samples $Sm_{1-x}Sr_xCoO_{3-\delta}$ with $x \leq 0.40$ annealed at 1100 °C in air for 300 h were double-phase.

Depending on the preparation conditions, Sr-enriched samples could be obtained either with tetragonal ($2a \times 2a \times 4a$)

Table 4

The synthesis conditions, structure type and unit cell parameters for the various $Sm_{1-x}Sr_xCoO_{3-\delta}$ compositions

Composition	Synthesis route	Final treatment conditions	Crystal structure and unit cell parameters	Ref.
$SmCoO_{3-\delta}$	ceramic route	1200 °C, in air	Orthorhombic a = 5.357(1), b = 5.294(1), c = 7.513(2)	[1]
$Sm_{0.9}Sr_{0.1}CoO_{3-\delta}$			Orthorhombic a = 5.363(1), b = 5.298(2), c = 7.518(3)	
$Sm_{0.8}Sr_{0.2}CoO_{3-\delta}$			Orthorhombic a = 5.361(1), b = 5.371(2), c = 7.577(2)	
$Sm_{0.75}Sr_{0.25}CoO_{3-\delta}$	nitrate route	800–1200 °C, in air, finally 1000 °C, 3 days	a = 10.877(1), c = 7.716(1)	[53]
$Sm_{0.7}Sr_{0.3}CoO_{3-\delta}$	ceramic route	1200 °C, in air	Orthorhombic a = 5.366(1), b = 5.377(2), c = 7.583(1)	[1]
$Sm_{0.6}Sr_{0.4}CoO_{3-\delta}$			Orthorhombic a = 5.369(2), b = 5.389(2), c = 7.588(2)	
$Sm_{0.5}Sr_{0.5}CoO_{3-\delta}$	ceramic route	1200 °C, in air	Orthorhombic a = 5.367(2), b = 5.406(1), c = 7.588(2)	[1]

Composition	Synthesis route	Final treatment conditions	Crystal structure and unit cell parameters	Ref.
$Sm_{0.5}Sr_{0.5}CoO_{3-\delta}$	nitrate route	1100 °C, in air	Orthorhombic a = 5.366(7), b = 5.370(9), c = 7.587(3)	[57]
	EDTA-citrate complexing sol-gel process	900 °C, in air	Orthorhombic *Pnma* a = 5.366, b = 5.398, c = 7.585	[58]
	ceramic route	1150 °C, in air	Cubic a = 3.8086(5)	[50]
	nitrate route	800–1200 °C, in air, finally 1000 °C, 3 days	Cubic a = 3.795(1)	[53]
	glycerin-nitrate route	1100 °C, in air	Tetragonal (2a×2a ×4a), *I4/mmm* a = 7.587(1), c = 15.253(1)	[59]
$Sm_{0.45}Sr_{0.55}CoO_{3-\delta}$	glycerin-nitrate route	1100 °C, in air	Tetragonal (2a×2a ×4a), *I4/mmm* a = 7.593(1), c = 15.333(1)	[59]
$Sm_{0.4}Sr_{0.6}CoO_{3-\delta}$	ceramic route	1150–1200 °C, in air	Cubic a = 3.808(2) a = 3.8178(5)	[1] [50]
	glycerin-nitrate route	1100 °C, in air	Tetragonal (2a×2a×4a), *I4/mmm* a = 7.582(1), c = 15.339(1)	[59]
$Sm_{0.35}Sr_{0.65}CoO_{3-\delta}$	glycerin-nitrate route	1100 °C, in air	Tetragonal (2a×2a×4a), *I4/mmm* a = 7.596(1), c = 15.328(1)	[59]
$Sm_{0.33}Sr_{0.67}CoO_{3-\delta}$	citrate-nitrate route	1100 °C, oxygen flow	Tetragonal (2a×2a×4a), *I4/mmm* a = 7.6149(4), c = 15.3472(10)	[54]
$Sm_{0.3}Sr_{0.7}CoO_{3-\delta}$	ceramic route	1150–1200 °C, in air	Cubic a = 3.823(2) a = 3.8306(1) a =3.830	[1] [50] [51]
	glycerin nitrate route	1100 °C, in air	Tetragonal (2a×2a×4a), *I4/mmm* a = 7.625(1), c = 15.368(1)	[59]
$Sm_{0.25}Sr_{0.75}CoO_{3-\delta}$	nitrate route	800–1200 °C, in air, finally 1000 °C, 3 days	Orthorhombic $GdFeO_3$ type a =5.363(1), b =5.353(1), c =7.592(1)	[53]
	glycerin nitrate route	1100 °C, in air	Tetragonal (2a×2a×4a), *I4/mmm* a = 7.631(1), c = 15.364(1)	[59]
$Sm_{0.2}Sr_{0.8}CoO_{3-\delta}$	citrate nitrate route	1100 °C, oxygen flow	Tetragonal (2a×2a×4a), *I4/mmm* a = 7.6724(4), c = 15.3983(11)	[54]
	ceramic route	1150–1200 °C, in air	Cubic a =3.846(2) a = 3.8407(3)	[1] [50]
	glycerin nitrate route	1100 °C, in air	Tetragonal (2a×2a×4a), *I4/mmm* a = 7.669(1), c = 15.405(1)	[59]

Composition	Synthesis route	Final treatment conditions	Crystal structure and unit cell parameters	Ref.
$Sm_{0.15}Sr_{0.85}CoO_{3-\delta}$	glycerin nitrate route	1100 °C, in air	Tetragonal (2*a*×2*a*×4*a*), *I*4/*mmm* *a* = 7.678(1), *c* = 15.372(1)	[59]
$Sm_{0.1}Sr_{0.9}CoO_{3-\delta}$	citrate nitrate route	1100 °C, oxygen flow	Tetragonal (2*a*×2*a*×4*a*), *I*4/*mmm* *a* = 7.6968(8), *c* = 15.4672(16)	[54]
	ceramic route	1150–1200 °C, in air	Cubic *a* = 3.848(2) *a* = 3.8531(4)	[1] [50]
	glycerin nitrate route	1100 °C, in air	Tetragonal (2*a*×2*a*×4*a*), *I*4/*mmm* *a* = 7.668(1), *c* = 15.410(1)	[59]
$Sm_{0.05}Sr_{0.95}CoO_{3-\delta}$	glycerin nitrate route	1100 °C, in air	Tetragonal (2*a*×2*a*×4*a*), *I*4/*mmm* *a* = 7.668(1), *c* = 15.431(1)	[59]

[54, 59] or cubic [1, 50] structure. One can see that the samples with the tetragonal structure appear in the relatively more oxidizing conditions and the samples with the cubic structures formed in the relatively more reducing conditions (Table 4). Fig. 8 illustrates the XRD pattern for $Sr_{0.8}Sm_{0.2}CoO_{3-\delta}$ with the $2a_p \times 2a_p \times 4a_p$ superstructure.

Electron diffraction measurements uncovered the formation of $2a_p \times 2a_p \times 4a_p$ superstructure (sp. gr. *I*4/*mmm*) within the tetragonal cell, but the intensity of reflections corresponding to the superstructure decreases with the increase of strontium content [54, 55]. The superstructure forms

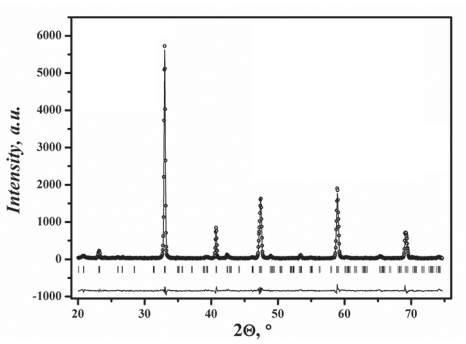

Fig. 8. XRD pattern for $Sr_{0.8}Sm_{0.2}CoO_{3-\delta}$ with the $2a_p \times 2a_p \times 4a_p$ superstructure [59]

because of the ordering of Sm and Sr cations in the A-site sublattice accompanied by the ordering of oxygen vacancies. For $Sr_{1-x}Sm_xCoO_{3-\delta}$ with $x < 0.25$, Sm atoms are first incorporated into the A1 position until substitution is complete, while the A2 and A3 sites remain fully occupied by Sr^{2+}. Further increase of samarium content leads to the incorporation of Sm cations into the A3 position, while A1 is fully occupied by Sm^{3+} and A2 is completely filled with Sr^{2+}. The value of Sm content, $x = 0.5$, corresponding to the limiting composition of solid solution, represents the situation when half of A3 positions are occupied by Sm^{3+} and the other half – by Sr^{2+} [54, 59].

Thermodynamic stability of the $Sm_{1-x}Sr_xCoO_{3-\delta}$ solid solutions has not been studied yet. Usually partial substitution of alkaline-earth elements for rare-earth in the cobaltites with the perovskite structure decreases their thermodynamic stability [60]. The only information concerning the behavior of $Sm_{0.5}Sr_{0.5}CoO_{3-\delta}$ under extremely reducing conditions at low temperature is available [61]. It was found that at 250 °C under 4% H_2O-96% H_2 atmosphere samarium-strontium cobaltite decomposes to SrO, $Co(OH)_2$ and CoO on the surface

of the reduced $Sm_{0.5}Sr_{0.5-\alpha}Co_{1-\beta}O_{3-\gamma}$ layer. In the atmosphere of pure H_2 at 350 °C $Sr_{0.5}Sm_{0.5}CoO_{3-\delta}$ completely decomposes into Sm_2O_3, SrO and CoO [61].

The solid solutions $Sm_{2-x}Sr_xCoO_4$ with K_2NiF_4 type structure (sp. gr. *I*4/*mmm*) within the range $0.8 \le x \le 1.50$ were prepared either by the conventional ceramic technique at 1200–1300 °C in air [56, 62], or at 1450 K in oxygen flow [63], or by the EDTA-citrate sol-gel method at 1000 °C in oxygen flow [64], or by the glycerin-nitrate technique at 1100 °C in air [59]. The homogeneity range of $Sm_{2-x}Sr_xCoO_4$ solid solutions, estimated by EDX analysis, was reported as $0.79 \le x \le 1.68$ [63]. The samples quenched in air from 1100 °C were single-phase within the range $0.7 \le x \le 1.1$ [59]. The unit cell parameters for $Sm_{2-x}Sr_xCoO_4$ are listed in Table 5.

Another representative of the Ruddlesden-Popper series $Sm_2SrCo_2O_7$ was reported earlier [64]. It was prepared from Sm_2O_3, $SrCO_3$ and Co_2O_3 by solid state synthesis at 1450 K in the flow of oxygen for 3 days [64]. According to the powder X-ray diffraction measurements, it possesses the tetragonal structure with the unit cell parameters: a = 0.3801 nm, c = 1.9562 nm, V = 0.2826 nm^3. It was shown that thermal stability of this phase is limited. The X-ray diffraction of the sample after heating at 1550 K for 6 h indicated that the compound decomposes to $SmSrCoO_4$ and $SmCoO_3$ [64]. It worth to mention that $Sm_2SrCo_2O_7$ formation was not confirmed during the systematic study of phase equilibria in the ½ Sm_2O_3 – SrO – CoO system at 1100 °C in air.

The projection of isothermal–isobaric phase diagram for the Sm – Sr – Co – O system to the compositional triangle ½ Sm_2O_3 – SrO – CoO is shown in Fig. 9 [59].

Table 5

The unit cell parameters and unit cell volumes for $Sm_{2-x}Sr_xCoO_4$ [59, 62, 63]

Sample composition	*a*, Å	*c*, Å	V, (Å)^3	Ref.
$Sm_{0.5}Sr_{1.5}CoO_{4-\delta}$	3.761	12.234	173.4	[62]
	3.7699(2)	12.4085(6)	176.35(1)	[63]
$Sm_{0.75}Sr_{1.25}CoO_{4-\delta}$	3.7620(2)	12.3575(8)	174.89(2)	[63]
$Sm_{0.8}Sr_{1.2}CoO_{4-\delta}$	3.753(1)	12.304(1)	173.36(2)	[59]
$Sm_{0.9}Sr_{1.1}CoO_{4-\delta}$	3.756(1)	12.266(1)	173.04(2)	[59]
$SmSrCoO_{4-\delta}$	3.7609(3)	12.2454(9)	173.20(2)	[63]
	3.752(1)	12.200(1)	171.76(2)	[59]
$Sm_{1.1}Sr_{0.9}CoO_{4-\delta}$	3.765(1)	12.198(1)	172.95(2)	[59]
$Sm_{1.2}Sr_{0.8}CoO_{4-\delta}$	3.768(1)	12.171(1)	172.77(2)	[59]
$Sm_{1.3}Sr_{0.7}CoO_{4-\delta}$	3.777(1)	12.180(1)	173.74(2)	[59]

Phase equilibria in Sm – Sr – Fe – O system

Three types of solid solutions were reported to exist in the Sm-Sr-Fe-O system: $Sm_{1-x}Sr_xFeO_{3-\delta}$ [56, 65–70], $Sm_{2-y}Sr_yFeO_{4\pm\delta}$ [56, 62], and $Sr_{3-z}Sm_zFe_2O_{7-\delta}$ [71].

Complex oxides with the overall composition $Sm_{1-x}Sr_xFeO_{3-\delta}$ may be prepared by solid state [66], glycine nitrate [56, 68, 70], EDTA-citrate sol-gel [7, 67, 69] or co-precipitation [56] methods at 900–1300 °C. All samples of $Sm_{1-x}Sr_xFeO_{3-\delta}$ solid solution range, whether as-prepared in air or treated at high oxygen pressure (100 bar at 600 °C

[66]), possess orthorhombically distorted perovskite type structure (sp. gr. *Pbnm*). The unit cell parameters for $Sm_{1-x}Sr_xFeO_{3-\delta}$ are listed in Table 6.

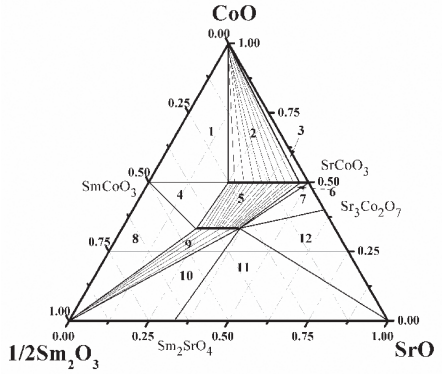

Fig. 9. The phase diagram of the ½ Sm_2O_3 – SrO – CoO system at 1100 °C in air: 1 – $SmCoO_3$, CoO, $Sr_{0.5}Sm_{0.5}CoO_{3-\delta}$; 2 – CoO, $Sr_{1-x}Sm_xCoO_{3-\delta}$ ($0.05 \le x \le 0.5$); 3 – CoO, $Sr_{0.95}Sm_{0.05}CoO_{3-\delta}$, $SrCoO_{3-\delta}$; 4 – $SmCoO_{3-\delta}$, $Sr_{0.5}Sm_{0.5}CoO_3$, $Sr_{0.7}Sm_{1.3}CoO_{4+\delta}$; 5 – $Sr_{1-x}Sm_xCoO_{3-\delta}$ ($0.05 \le x \le 0.5$), $Sr_{2-y}Sm_yCoO_{4+\delta}$ ($0.9 \le y \le 1.3$); 6 – $Sr_{1.1}Sm_{0.9}CoO_{4+\delta}$, $SrCoO_{3-\delta}$, $Sr_{0.95}Sm_{0.05}CoO_{3-\delta}$, $SrCoO_{3-\delta}$; 7 – $SrCoO_{3-\delta}$, $Sr_3Co_2O_{7-\delta}$, $Sr_{1.1}Sm_{0.9}CoO_{4+\delta}$; 8 – Sm_2O_3, $SmCoO_{3-\delta}$, $Sr_{0.7}Sm_{1.3}CoO_{4+\delta}$; 9 – $Sr_{2-y}Sm_yCoO_{4+\delta}$ ($0.9 \le y \le 1.3$), Sm_2O_3; 10 – Sm_2O_3, $Sm_2SrO_{4-\delta}$, $Sr_{1.1}Sm_{0.9}CoO_{4+\delta}$; 11 – SrO, $Sm_2SrO_{4-\delta}$, $Sr_{1.1}Sm_{0.9}CoO_{4+\delta}$; 12 – SrO, $Sr_3Co_2O_{7-\delta}$, $Sr_{1.1}Sm_{0.9}CoO_{4+\delta}$ [59]

Single-phase $Sr_{2-y}Sm_yFeO_{4\pm\delta}$ samples were synthesized by the glycine nitrate route [56] or by the solid-state technique [62] with the final annealing temperature within the range 1000–1250 °C. The homogeneity range of $Sr_{2-y}Sm_yFeO_{4\pm\delta}$ solid solution was reported to be equal to $0.5 \le y \le 1.2$ [62].

$Sr_{3-z}Sm_zFe_2O_{7-\delta}$ solid solutions were synthesized by the glycine-nitrate method at 1100 °C in air [71]. It was shown that single-phase $Sr_{3-z}Sm_zFe_2O_{7-\delta}$ formed in the composition range $0 \le z \le 0.3$ and at $z = 1.80$. Similarly to the undoped $Sr_3Fe_2O_{7-\delta}$, partially Sm-substituted $Sr_{3-z}Sm_zFe_2O_{7-\delta}$ (z =0–0.3) possesses the tetragonal structure (sp. gr. *I4/mmm)*. Sm-enriched single phase $Sr_{1.2}Sm_{1.8}Fe_2O_{7-\delta}$ also crystallizes in the tetragonal system, although the space group is different ($P4_2/mnm$).

All attempts to synthesize Sm-substituted strontium hexaferrite $Sr_{1-z}Sm_zFe_{12}O_{19}$ ($0.06 \le z \le 0.5$) solid solutions by hydrothermal [10, 11] or solid state [12] methods failed. It was found that all Sm-containing powders were multiphase; together with $SrFe_{12}O_{19}$ they contained Fe_2O_3 and (Sm, Sr)$FeO_{3-\delta}$ as the impurity phases.

Table 6

The unit cell parameters for the $Sr_{1-x}Sm_xFeO_{3-\delta}$ solid solution

x	Structure	a, Å	b, Å	c, Å	Ref.
0.5	Orthorhombic sp. gr. *Pbnm*	5.4622(1)	5.4627(4)	7.7249(1)	[70]
0.667		5.4728(2)	5.4454(2)	7.6973(2)	[66]
0.8		5.396	5.562	7.711	[69]

Phase equilibrium in Sm – Ba – Co – O system

Relatively large difference in ionic radii between samarium and barium, in comparison with that between samarium and strontium, results in the formation of so-called "112 type" phase with the formula $SmBaCo_2O_{6-\delta}$ [72–74] instead of solid solution that is typical for the Sr-containing system. The structure of $SmBaCo_2O_{6-\delta}$ is also called as double perovskite since Sm and Ba atoms are separated to the alternating layers along the c axis. Therefore, the value of the c parameter is doubled

relatively to the ordinary perovskite structure, and the unit cell can be represented as $a_p \times a_p \times 2a_p$. Another specific feature of this structure that is caused by the cation separation is the location of oxygen vacancies. It is generally acknowledged that oxygen vacancies are not distributed randomly in the lattice while the oxygen content changes within the range $5 < (6-\delta) < 6$, but are concentrated in the particular planes. According to the most widespread point of view, oxygen vacancies are located in the SmO_δ planes while BaO planes remain completed [74–76], however, alternatively the opposite model was suggested in [77]. Such accumulation of oxygen vacancies in the specific planes (doesn't matter what they are – either SmO_δ or BaO_δ) results in the ordering of oxygen vacancies when the value of $(6-\delta)$ is equal approximately to 5.5, leading to the doubling of *b*-parameter and formation of the $a_p \times 2a_p \times 2a_p$ supercell.

$SmBaCo_2O_{6-\delta}$ can be prepared by a conventional ceramic technique [3, 74, 78–81] and via solution methods using different precursors [82–84]. It possesses the orthorhombic structure (space group *Pmmm*) with the $a_p \times 2a_p \times 2a_p$ supercell. The value of oxygen content at room temperature in the sample slowly cooled in air was found to be 5.61 [81]. This value corresponds to the orthorhombic structure. The X-ray diffraction pattern for $SmBaCo_2O_{5.61}$ refined by the Rietveld analysis is shown in Fig. 10 and the structural parameters are listed in Table 7.

The samples within the compositional range $Sm_{1-x}Ba_xCoO_{3-\delta}$ with $x < 0.5$ annealed at 1100 °C in air were double-phase and consisted of $SmBaCo_2O_{5.61}$ and $SmCoO_{3-\delta}$, while the samples with $x > 0.5$ were the mixtures of $SmBaCo_2O_{5.61}$ and $BaCoO_{3-\delta}$ [72, 73].

High temperature *in situ* XRD measurements reveals the structural transfor-

Table 7

The unit cell parameters and atomic coordinates for $SmBaCo_2O_{5.61}$ [81]

Space group *Pmmm*			
atom	*x*	*y*	*z*
Sm	0.5	0.229(3)	0.5
Ba	0.5	0.250(1)	0
Co1	0	0.5	0.255(2)
Co2	0	0	0.254(2)
O1	0	0	0
O2	0	0.5	0
O3	0	0.5	0.5
O4	0	0	0.5
O5	0.5	0	0.239(3)
O6	0.5	0.5	0.247(3)
O7	0	0.244(2)	0.238(2)

$a = 3.886(1)$ Å; $b = 7.833(1)$ Å; $c = 7.560(1)$ Å;
$V = 230.22(2)$ (Å)^3;
$R_{Br} = 10.7\%$; $R_p = 7.73\%$; $R_{exp} = 4.46\%$

mation from orthorhombic to tetragonal cell between 450 and 550 °C (Fig. 11) that is in good agreement with the value of oxygen content in $SmBaCo_2O_{6-\delta}$ within this temperature range. Temperature dependence of unit cell parameters for $SmBaCo_2O_{6-\delta}$ is shown in Fig. 12.

Although the radius of samarium is significantly larger than radius of cobalt ions, it was found that the solid solutions represented by the formula $BaCo_{1-z}Sm_zO_{3-\delta}$ can be prepared by citrate-nitrate method at 1100 °C in air within the range $0.1 \leq z \leq 0.2$. Partial substitution of Sm for Co stabilized the cubic structure similarly to $BaCo_{1-z}Y_zO_{3-\delta}$ [85]. Fig. 13 illustrates XRD pattern for the single-phase cubic solid solution $BaCo_{0.85}Sm_{0.15}O_{3-\delta}$ as an example. The unit cell parameters refined by the Rietveld method are listed in Table 8. The sample with nominal composition $z = 0.05$ consisted of cubic $BaCo_{0.9}Sm_{0.1}O_{3-\delta}$ and hexagonal $BaCoO_{3-\delta}$.

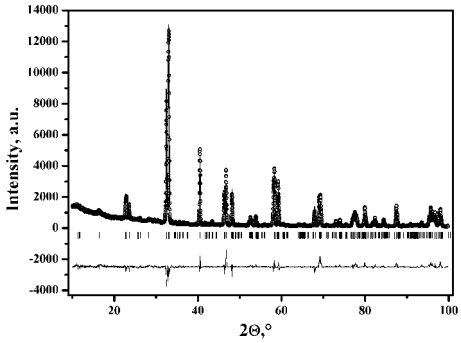

Fig. 10. The X-ray diffraction pattern for $SmBaCo_2O_{5.61}$, refined by the Rietveld method [72]

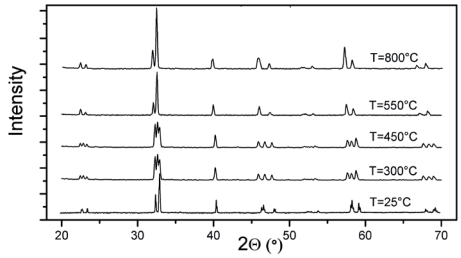

Fig. 11. High-temperature in situ diffraction data for $SmBaCo_2O_{6-\delta}$ [84]

One more complex oxide with the formula $Sm_2BaCo_2O_7$ representing the Ruddlesden-Popper (RP) (n=2) phase was reported to exist in the Sm – Ba – Co – O system [63, 86]. It was obtained by solid-state reaction from Sm_2O_3, $BaCO_3$ and Co_2O_3 at 1300 K in the flow of oxygen for 2 weeks. The crystal structure was described by the orthorhombic cell with the parameters a = 3.821 Å, b = 3.776 Å and c = 19.426 Å [85]. However, Gillie et al. [87] using same preparation method with prolonged annealing in flowing oxygen at 1100 °C did not obtain the single phase but the mixture composed of two distinct phases: an oxy-

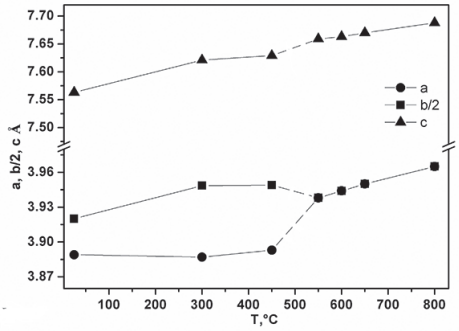

Fig. 12. Temperature dependencies of the unit cell parameters and unit cell volume for $SmBaCo_2O_{6-\delta}$ in air [84]

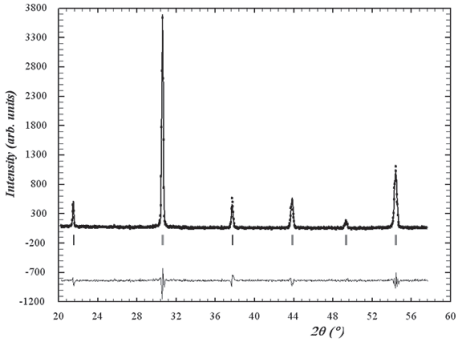

Fig. 13. XRD pattern for the cubic solid solution $BaCo_{0.85}Sm_{0.15}O_{3-\delta}$, refined by the Rietveld method [72]

genated 112-type phase $SmBaCo_2O_{5+x}$ ($x \approx 0.5$), and double-layered RP target compound. From a set of obtained results it was concluded that the composition of RP phase is probably close to $Sm_{2.1}Ba_{0.8}Co_{2.1}O_{7-\delta}$ (where $\delta \approx 1$). The unit cell parameters refined within the *Pnnm* space group were equal to a = 5.4371(4) Å, b = 5.4405(4) Å, and c = 19.8629(6) Å [87].

The only one complex oxide $Sm_2BaO_{4\pm\delta}$ was described in the Sm – Ba – O system [73, 88, 89]. It can be prepared as a single phase by a conventional ceramic technique at 1500 °C in air for about 24 h [88]. $Sm_2BaO_{4\pm\delta}$ demonstrates low stability at room temperature due to high hygroscopicity and reactivity with CO_2 [88, 89]. However, DTA curves in the temperature range 950–1400 °C in air indicated no phase transitions occurred. The presumed space group is *Pbna* with the lattice parameters a = 12.313 Å, b = 10.535 Å, c = 3.564 Å [88]. The standard Gibbs energy of Sm_2BaO_4 formation from the binary oxides Sm_2O_3 and BaO, determined by the high-temperature CaF_2-based EMF method, was evaluated as –110 kJ/mol at 1100 K [89].

According to the XR results, partial dissolution of BaO in Sm_2O_3 at 1100 °C in air was about 15 mol% [72]. The unit cell parameters for the $Sm_{2-x}Ba_xO_3$ solid solutions are listed in Table 9.

The phase diagram for the Sm – Ba – Co – O system at 1100 °C in air [72] is shown in Fig. 14. According to the obtained results, it could be assumed that RP phase is thermodynamically unstable at 1100 °C in air but could be synthesized in more oxidizing conditions.

Phase equilibria in Sm – Ba – Fe – O system

In contrast with $SmBaCo_2O_{6-\delta}$, similar samarium-barium ferrite $SmBaFe_2O_{6-\delta}$ with the double perovskite structure can be obtained only under reduction conditions. Karen et al. [90, 91] synthesized $SmBaFe_2O_{6-\delta}$ at 985–1020 °C in atmosphere with oxygen partial pressure pO_2 about $10^{-14.88}$–$10^{-15.5}$ bar that was achieved by

Table 8

The unit cell parameters for $BaCo_{1-z}Sm_zO_{3-\delta}$, refined by the Rietveld method [72]

z	a, Å	V, (Å)^3	R_B,%	R_f,%	R_p,%
0.1	4.108(1)	69.33(1)	2.04	1.72	13.4
0.15	4.131(1)	70.51(1)	1.59	1.50	9.76
0.2	4.143(1)	71.13(2)	1.30	1.09	16.4

Table 9

The unit cell parameters for the $Sm_{2-x}Ba_xO_3$ solid solutions

$Sm_{2-x}Ba_xO_3$ Space group *C2/m*							
x	a, Å	b, Å	c, Å	V, (Å)^3	R_B,%	R_f,%	R_p,%
0.05	14.191(1)	3.628(1)	8.860(1)	449.22(2)	1.27	1.15	10.2
0.1	14.180(1)	3.626(1)	8.855(1)	448.39(1)	3.20	2.45	13.9
0.2	14.177(1)	3.625(1)	8.853(1)	448.08(1)	2.40	2.21	13.7
0.3	14.175(1)	3.625(1)	8.851(1)	447.92(2)	1.82	2.01	13.3

mixing of hydrogen, argon or oxygen and water vapor. Moritomo et al. [92] prepared $SmBaFe_2O_{6-\delta}$ at 985 °C for 40 h in an evacuated fused-silica tube with Fe metal grains put inside the tube, which served as a getter mixture (Fe/FeO) and provided the oxygen partial pressure of about 7.6×10^{-16} atm. Although it is impossible to prepare $SmBaFe_2O_{6-\delta}$ in air, it remains single-phase after annealing at 900 °C in air [93] or even at 985°C in pure oxygen [91].

The crystal structure of $SmBaFe_2O_{6-\delta}$ is well described within the tetragonal or the orthorhombic unit cell ($a_p\times a_p\times 2a_p$), depending on the oxygen content [90–93]. Similarly to the Co-containing double perovskite, the appearance of the ($a_p\times 2a_p\times 2a_p$) supercell takes place in the vicinity of oxygen content equal to 5.5. The values of unit cell parameters and synthesis conditions for $SmBaFe_2O_{6-\delta}$ are listed in Table 10.

The complex oxide $SmBa_2Fe_3O_{8+\delta}$ can be obtained at 500 °C in oxygen flow [93] or at 1100 °C for 200 h [94]. The structural refinements were performed by the Rietveld method within the ideal perovskite cubic structure (space group *Pm*3*m*).

The only single-phase sample $Sm_{0.375}Ba_{0.625}FeO_{3-\delta}$ was prepared at 1100 °C in air [95, 96] and described within a cubic unit cell (space group *Pm*3*m*) with a = 3.934(1) Å. However, transmission electron microscopy revealed that $Sm_{0.375}Ba_{0.625}FeO_{3-\delta}$ possesses tetragonal structure with 5-fold c parameter $a_p\times a_p\times 5a_p$. Such complex structure is formed by alternation of the layers containing exclusively samarium and barium with the mixed layers, as follows: Sm–Ba– (Sm, Ba)–(Sm, Ba)–Ba–Sm [95, 96] (Fig. 15).

Table 10

The values of unit cell parameters and synthesis conditions for $SmBaFe_2O_{6-\delta}$ [90]

6–δ	*a*, Å	*b*, Å	*c*, Å	structure	Ar/H_2	$\log(pH_2O)$	$\log(pO_2)$	*T*, °C
4.980	3.963	3.946	7.609	orthorhombic $a_p\times a_p\times 2a$ (sp.gr. *Pmmm*)	8.78	–4.1	–27.6	670
4.999	3.963	3.945	7.612		8.65	–4.4	–29.3	630
5.002	3.962	3.945	7.611		8.65	–4.2	–28.6	640
5.007	3.962	3.944	7.611		8.65	–4.3	–29.4	620
5.014	3.962	3.946	7.612		8.78	–4.1	–27.9	660
5.016	3.963	3.946	7.612		8.78	–4.1	–28.2	650
5.022	3.962	3.944	7.617		8.78	–4.1	–28.5	640
5.030	3.959	3.948	7.621		16.3	–1.68	–15.31	1000
5.064	3.953		7.628	tetragonal (sp.gr *P*4/*mmm*) $a_p\times 2a_p\times 2a$	24.9	–1.67	–14.93	1000
5.095	3.952		7.636		41.3	–1.68	–14.53	1000
5.137	3.949		7.649		74.2	–1.68	–14.03	1000
5.142	3.950		7.654		83.2	–1.64	–13.85	1000
5.182	3.949		7.664		101	–1.68	–13.76	1000
5.202	3.947		7.671		137	–1.69	–13.51	1000
5.249	3.946		7.686		238	–1.66	–12.96	1000
5.320	3.943		7.705		398	–1.62	–12.44	1000
5.346	3.943		7.714		341	–1.65	–12.64	1000

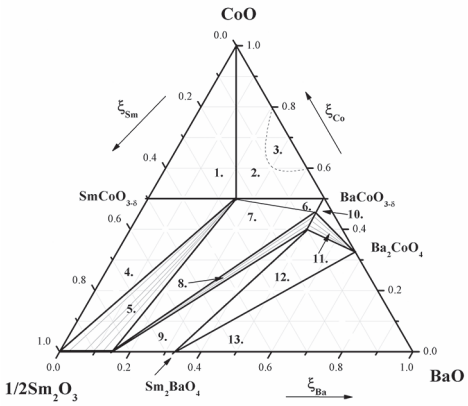

Fig. 14. A projection of isobaric-isothermal phase diagram of the Sm–Ba–Co–O system to the metallic components triangle (T = 1100 °C, pO_2 = 0.21 atm): 1 – $SmCoO_{3-\delta}$, CoO and $SmBaCo_2O_{6-\delta}$; 2 – CoO, $SmBaCo_2O_{6-\delta}$ and $BaCoO_{3-\delta}$; 3 – melt; 4 – Sm_2O_3, $SmCoO_{3-\delta}$ and $SmBaCo_2O_{6-\delta}$; 5 – $SmBaCo_2O_{6-\delta}$ and $Sm_{2-x}Ba_xO_{3-\delta}$ ($0 \le x \le 0.3$); 6 – $SmBaCo_2O_{6-\delta}$, $BaCoO_{3-\delta}$ and $BaCo_{0.9}Sm_{0.1}O_{3-\delta}$; 7 – $SmBaCo_2O_{6-\delta}$, $BaCo_{0.9}Sm_{0.1}O_{3-\delta}$ and $Sm_{1.7}Ba_{0.3}O_{3-\delta}$; 8 – $Sm_{1.7}Ba_{0.3}O_{3-\delta}$ and $BaCo_{1-z}Sm_zO_{3-\delta}$ ($0.1 \le z \le 0.2$); 9 – $Sm_{1.7}Ba_{0.3}O_{3-\delta}$, Sm_2BaO_4 and $BaCo_{0.8}Sm_{0.2}O_{3-\delta}$; 10 – $BaCoO_{3-\delta}$, Ba_2CoO_4 and $BaCo_{0.9}Sm_{0.1}O_{3-\delta}$; 11 – Ba_2CoO_4 and $BaCo_{1-z}Sm_zO_{3-\delta}$ ($0.1 \le z \le 0.2$); 12 – Sm_2BaO_4, Ba_2CoO_4 and $BaCo_{0.8}Sm_{0.2}O_{3-\delta}$; 13 – Sm_2BaO_4, Ba_2CoO_4 and BaO [72]

Phase equilibrium in Sm – Co – Fe – O system

The solid solutions between samarium ferrite and samarium cobaltite $SmFe_{1-x}Co_xO_{3-\delta}$ were extensively studied [52, 97–102] because of their possible application as gas sensors. Polycrystalline samples of $SmFe_{1-x}Co_xO_{3-\delta}$ can be prepared by the pyrolysis of cyanide complexes [97, 99], sol–gel method [98, 100, 102] or conventional solid-state technique [52] at 800–1100 °C. It was shown that the homogeneity range of $SmFe_{1-x}Co_xO_{3-\delta}$ solid solutions extended to the entire range of compositions ($0 \le x \le 1$). Similarly to the undoped parent oxides $SmFeO_{3-\delta}$ and $SmCoO_{3-\delta}$, the structure of all $SmFe_{1-x}Co_xO_{3-\delta}$ solid solutions was identified as orthorhombic. The unit cell parameters and unit cell volume values are listed in Table 11 [98, 102].

Another solid solution in the Sm – Fe – Co – O system was obtained by partial substitution of Sm for Fe in the cobalt ferrite $CoFe_2O_4$ with spinel structure [103–107]. The solid oxides with overall composition $CoFe_{2-y}Sm_yO_4$ were prepared at 400–1000 °C by co-precipitation [103–105] or sol-gel decomposition [105, 107] methods. Single-phase samples $CoFe_{2-y}Sm_yO_4$ were obtained at temperatures 400–700 °C within the ranges $0 \le y \le 0.2$ [105] and $0 \le y \le 0.4$ [107] by sol-gel technology or

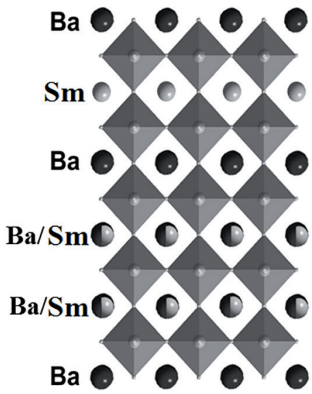

Fig. 15. Crystal structure of five-layered ordered perovskite $Sm_{1.875}Ba_{3.125}Fe_5O_{15-\delta}$ [95, 96]

Table 11

The unit cell parameters and unit cell volume of the $SmFe_{1-x}Co_xO_{3-\delta}$ solid solutions [98, 102]

x	a, Å	b, Å	c, Å	V, Å^3	Ref.
0	5.5871	7.6977	5.3852	231.61	[98]
	5.400	5.593	7.708	232.83	[102]
0.1	5.8551	7.5196	5.0739	223.40	[98]
	5.390	5.557	7.691	231.19	[102]
0.2	5.8421	7.4964	5.0670	221.91	[98]
	5.378	5.554	7.668	229.01	[102]
0.3	5.7916	7.4653	5.0618	218.85	[98]
	5.364	5.520	7.634	226.03	[102]
0.4	5.7812	7.4689	5.0533	218.20	[98]
	5.363	5.448	7.620	224.26	[102]
0.5	5.7189	7.4671	5.0649	216.29	[98]
	5.340	5.453	7.584	220.83	[102]
0.6	5.324	5.422	7.554	218.09	[102]
0.7	5.316	5.412	5.548	217.17	[102]
0.8	5.6564	7.3754	4.9933	208.31	[98]
	5.308	5.394	7.536	215.76	[102]
0.9	5.297	5.371	5.518	213.91	[102]
1.0	5.5148	7.2953	4.9582	199.48	[98]
	5.286	5.353	7.499	212.18	[102]

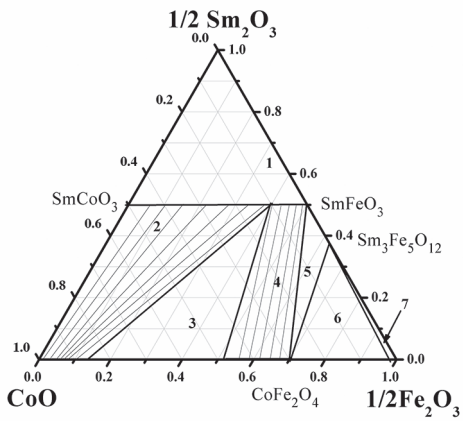

Fig. 16. A projection of isobaric-isothermal phase diagram for the Sm–Fe–Co–O system to the compositional triangle (T = 1100 °C, pO_2 = 0.21 atm): 1 – Sm_2O_3, $SmFe_{1-x}Co_xO_{3-\delta}$ ($0 \le x \le 1.0$); 2 – $Co_{1-u}Fe_uO$ ($0 \le u \le 0.13$), $SmFe_{1-x}Co_xO_{3-\delta}$ ($0.2 \le x \le 1.0$); 3 – $Co_{0.87}Fe_{0.13}O$, $Co_{1.35}Fe_{1.65}O_4$, $SmFe_{0.8}Co_{0.2}O_{3-\delta}$; 4 – $SmFe_{1-x}Co_xO_{3-\delta}$ ($0 \le x \le 0.2$), $Co_{1+v}Fe_{2-v}O_4$ ($-0.1 \le v \le 0.35$); 5 – $SmFeO_3$, $Sm_3Fe_5O_{12}$, $Co_{0.9}Fe_{2.1}O_4$; 6 – $Sm_3Fe_5O_{12}$, $Co_{0.9}Fe_{2.1}O_4$, $Fe_{1.985}Co_{0.015}O_3$; 7 – $Sm_3Fe_5O_{12}$, $Fe_{2-w}Co_wO_3$ ($0 \le w \le 0.03$) [102]

within the range $0 \leq y \leq 0.5$ [106] by co-precipitation by sodium hydroxide with following annealing at 800 °C. However, further increase of temperature (> 800 °C) led to the decomposition of $CoFe_{2-y}Sm_yO_4$ ($y > 0.1$ [105, 107] or $y \geq 0.3$ [106]) with a decrease in Sm content and formation of $SmFeO_3$ as a secondary phase. The increase of calcination temperature up to 1000 °C resulted in the complete decomposition of the $CoFe_{2-y}Sm_yO_4$ solid solution even with $y = 0.1$ [107].

The phase equilibria in the Sm–Fe–Co–O system at $T = 1100$ °C in air is presented in Fig. 16 [102] in the form of the isothermal-isobaric projections to the compositional triangle.

References

1. Tu HY, Takeda Y, Imanishi N, Yamamoto O. $Ln_{1-x}Sr_xCoO_3$ (Ln = Sm, Dy) for the electrode of solid oxide fuel cells. *Solid State Ionics*. 1997;100:283–8. DOI: 10.1016/S0167-2738(97)00360-3.
2. Kim J-H, Manthiram A. $LnBaCo_2O_{5+d}$ oxides as cathodes for intermediate-temperature solid oxide fuel cells. *J Electrochem Soc*. 2008;155: B385–90. DOI: 10.1149/1.2839028.
3. Zhou Q, He T, Ji Y. $SmBaCo_2O_{5+x}$ double-perovskite structure cathode material for intermediate-temperature solid-oxide fuel cells. *J Power Sources*. 2008;185:754–8. DOI: 10.1016/j.jpowsour.2008.07.064.
4. Chen D, Wang F, Shi H, Ran R, Shao Z. Systematic evaluation of Co-free $LnBaFe_2O_{5+1}$ (Ln = Lanthanides or Y) oxides towards the application as cathodes for intermediate-temperature solid oxide fuel cells. *Electrochimica Acta*. 2012;78:466–74. DOI: 10.1016/j.electacta.2012.06.073.
5. Kim J-H, Manthiram A. Characterization of $Sr_{2.7}Ln_{0.3}Fe_{1.4}Co_{0.6}O_7$ (Ln=La, Nd, Sm, Gd) intergrowth oxides as cathodes for solid oxide fuel cells. *Solid State Ionics*. 2009;180:1478–83. DOI: 10.1016/j.ssi.2009.09.007.
6. Chavez E, Mueller M, Mogni L, Caneiro A. Study of $LnBaCo_2O_{6-d}$ (Ln=Pr, Nd, Sm and Gd) double perovskite as new cathode material for IT-SOFC. *J Phys: Conf Ser*. 2009;167(012043):1–6. DOI: 10.1088/1742-6596/167/1/012043.
7. Li Q, Zhu X, Yang W. Single-step fabrication of asymmetric dual-phase composite membranes for oxygen separation. *J Membr Sci*. 2008;325:11–5. DOI: 10.1016/j.memsci.2008.08.002.
8. Kovalevsky AV, Kharton VV, Tikhonovich VN, Naumovich EN, Tonoyan AA, Reut OP, Boginsky LS. Oxygen permeation through $Sr(Ln)CoO_{3-\delta}$ (Ln=La, Nd, Sm, Gd) ceramic membranes. *Mater Sci Eng*. 1998; B52:105–16. DOI: 10.1016/S0921-5107(97)00292-4.
9. Ikeguchi M, Mimura T, Sekine Y, Kikuchi E, Matsukata M. Reaction and oxygen permeation studies in $Sm_{0.4}Ba_{0.6}Fe_{0.8}Co_{0.2}O_{3-d}$ membrane reactor for partial oxidation of methane to syngas. *Appl Catal, A*. 2005;290:212–20. DOI: 10.1016/j.apcata.2005.05.033.
10. Lechevalliera L, Le Breton JM, Wang JF, Harris IR. Structural analysis of hydrothermally synthesized $Sr_{1-x}Sm_xFe_{12}O_{19}$ hexagonal ferrites. *J Magn Magn Mater*. 2004;269:192–6. DOI: 10.1016/S0304-8853(03)00591-2.

11. Wang JF, Ponton CB, Harris IR. A study of Sm-substituted SrM magnets sintered using hydrothermally synthesized powders. *J Magn Magn Mater.* 2006;298:122–31. DOI: 10.1016/j.jmmm.2005.03.012.
12. Lechevallier L, Le Breton JM, Morel A, Teillet J. Structural and magnetic properties of $Sr_{1-x}Sm_xFe_{12}O_{19}$ hexagonal ferrites synthesised by a ceramic process. *J Alloys Compd*. 2003;359:310–4. DOI: 10.1016/S0925-8388(03)00206-8.
13. Arakawa T, Tsuchi-ya S-ishi, Shiokawa J. Catalytic properties and activity of rare earth orthoferrites in oxidation of methanol. *J Catal.* 1982;74:317–22. DOI: 10.1016/0021-9517(82)90037-9.
14. Li L, Wang X, Zhang Y. Enhanced visible light-responsive photocatalytic activity of $LnFeO_3$ (Ln = La, Sm) nanoparticles by synergistic catalysts. *Mater Res Bull*. 2014;50:18–22. DOI: 10.1016/j.materresbull.2013.10.027.
15. Sazonov LA, Moskvina ZV, Artamonov EV. Investigation of catalytic properties of compounds $LnMeO_3$ type in the reactions of homomolecular exchange of oxygen. *Kinet Catal*. 1974;15(1):120–6.
16. Arakawa T, Yoshida A, Shiokawa J. Catalytic properties of rare earth cobaltites and related compounds. *Mater Res Bull*. 1980;15(3):347–52. DOI: 10.1016/0025-5408(80)90178-6.
17. Michel CR, Delgado E, Santillán G, Martínez AH, Chávez-Chávez A. An alternative gas sensor material: Synthesis and electrical characterization of $SmCoO_3$. *Mater Res Bull.* 2007;42:84–93. DOI: 10.1016/j.materresbull.2006.05.008.
18. Delgado E, Michel CR. CO_2 and O_2 sensing behavior of nanostructured barium – doped $SmCoO_3$. *Mater Lett.* 2006:60;1613–6. DOI: 10.1016/j.matlet.2005.11.080.
19. Mochinaga R, Yamasaki T, Arakawa T. The gas-sensing of $SmCoO_X/MO_X$ (M=Fe, Zn, In, Sn) having a heterojunction. *Sens Actuators, B: Chemical.* 1998;52(1–2):96–9. DOI: 10.1016/S0925-4005(98)00262-7.
20. Kropanev AYu, Petrov AN, Zhukovsky VM. The phase diagrams of the Ln – Co – O systems (Ln = Sm, Eu, Gd, Tb, Dy, Ho). *Russ J Inorg Chem.* 1983;28(11):2938–43.
21. Kropanev AYu, Petrov AN. Thermal stability of $SmCoO_3$, $EuCoO_3$, $GdCoO_3$, $TbCoO_3$, $DyCoO_3$, $HoCoO_3$ cobaltites in air. *Inorg Mater.* 1983;19(12):1782–5.
22. Kitayama K. Thermogravimetric study of the Ln_2O_3-Co-Co_2O_3 system III. Ln=Pr, Sm, Eu and Tb. *J Solid State Chem*. 1988;77(2): 366–75. DOI: 10.1016/0022-4596(88)90260-5.
23. Wold A, Ward R. Perovskite type oxides of cobalt, chromium and vanadium with some rare earth elements. *J Am Chem Soc*. 1954;76(4):1029–30. DOI: 10.1021/ja01633a031.
24. Bertaut F, Forrat F. Sur les deformations dans les perovskites a base de terres rares et d'elements de transition trivalents. *J Phys Radium*. 1956;17:129–31. DOI: 10.1051/jphysrad:01956001702012900.
25. Kappatsch A, Qezel-Ambrunaz S, Sivardiere J. Structure et properties magnetiques des orthocobaltites de terres rares $TCoO_3$. *J Phys France*. 1970;31(4):369–76. DOI: 10.1051/jphys:01970003104036900.

26. Demazeau G, Pouchard M, Hagenmuller P. Sur de nouveaux composes oxygenes du cobalt +III derives de la perovskite. *J Solid State Chem*. 1974;9(3):202–9. DOI: 10.1016/0022–4596(74)90075–9.
27. Demazeau G, Pouchard M, Hagenmuller P. Les composes oxygenes ternaries du cobalt +3 et des terres. *C r Acad Sci.* 1973;277(2):109–12.
28. Pérez-Cacho J, Blasco J, García J, Sanchez R. Relationships between Structure and Physical Properties in $SmNi_{1-x}Co_xO_3$. *J Solid State Chem*. 2000;150:145–53. DOI: 10.1006/jssc.1999.8570.
29. Petrov AN, Kropanev AYu, Zhukovsky VM, Cherepanov VA, Neudachina GK. The conditions and mechanism of solid state synthesis of the rare earth cobaltates $RCoO_3$ (R=La, Pr, Nd, Sm, Gd). *Zhurnal Neorganicheskoi Khimii*. 1981;26(12):3190–4.
30. Kropanev AYu, Petrov AN, Rabinovich LYa. Investigations of solid state interactions of Ln_2O_3 with CoO (Ln = Sm, Eu, Gd, Dy, Ho). *Zhurnal Neorganicheskoi Khimii.* 1983;28(10):2609–12.
31. Kropanev AYu, Petrov AN, Rabinovich LYa. Solid state synthesis of RE cobaltites with $RCoO_3$ composition (R – Sm, Eu. Gd). *Inorg Mater* 1984;20(1):116–20.
32. Kniga MV, Akhrem LI. Kinetics of reaction of samarium oxide and cobalt oxide. *Izv AN BSSR Ser Khim Nauk.* 1968;2:56–60.
33. Petrov AN, Kropanev AYu, Zhukovsky VM. Thermodynamic properties of rare earth cobaltites with composition $RCoO_3$. *Zhurnal Fizicheskoj Khimii.* 1984;58(1):50–3.
34. Sabasri R, Pankajavalli R, Sreedharan OM. High temperature thermodynamic stabilities of $RCoO_3$ (R=Nd, Sm, Eu, Gd or Dy) using solid oxide-electrolyte emf technique. *J Alloy Compd.* 1998;269:71–4. DOI: 10.1016/S0925-8388(98)00004-8.
35. Kitayama K, Katsura T. Phase equilibria in Fe-Fe_2O_3-Ln_2O_3 (Ln=Sm and Er) systems at 1200 °C. *Bull Chem Soc Jpn*. 1976;49(4):998–1001. DOI: 10.1246/bcsj.49.998.
36. Parida SC, Jacob KT, Venugopal V. Thermodynamic Properties of $SmFeO_3$(s) and $Sm_3Fe_5O_{12}$ (s). *J Phase Equilibria.* 2003;24(5):431–40. DOI: 10.1361/1054971037.
37. Geller S, Wood EA. Crystallographic studies of perovstite-like compounds. I. Rare earth orthferrites and $YFeO_3$, $YCrO_3$, $YAlO_3$. *Acta Crystallogr.* 1956;9:563–8. DOI: 10.1107/S0365110X56001571.
38. Marezio M, Remeika JP, Dernier PD. The crystal chemistry of the rare earth orthoferrites. *Acta Crystallogr.* 1970; B26:2008–22. DOI: 10.1107/S0567740870005319.
39. Berenov A, Angeles E, Rossiny J, Raj E, Kilner J, Atkinson A. Structure and transport in rare-earth ferrates. *Solid State Ionics*. 2008;179:1090–3. DOI: 10.1016/j.ssi.2008.01.025.
40. Porta P, Cimino S, De Rossi S, Faticanti M, Minelli G, Pettiti I. $AFeO_3$ (A=La, Nd, Sm) and $LaFe_{1-x}Mg_xO_3$ perovskites: structural and redox properties. *Mater Chem Phys*. 2001;71:165–73. DOI: 10.1016/S0254–0584(01)00273–5.
41. Niu X, Li H, Liu G. Preparation, characterization and photocatalytic properties of $REFeO_3$ (RE = Sm, Eu, Gd). *J Mol Catal A: Chem*. 2005;232:89–93. DOI: 10.1016/j.molcata.2005.01.022.
42. Espinosa GP. Crystal chemistry study of the rare-earth iron garnets. *J Chem Phys*. 1962;10:2344–7. DOI: 10.1063/1.1733008.

43. Narayanan VKS, Gajbhiye NS, Bahadur D. Characterization of dysprosium and samarium iron garnets synthesized by the citrate gel process. *J Mater Sci Lett*. 1987;6:281–4. DOI: 10.1007/BF01729325.
44. Guillot M, Rodic D, Mitric M. Temperature dependencies of the lattice constants and thermal expansion coefficients of $Sm_3Fe_5O_{12}$ and $Er_3Fe_5O_{12}$ single crystals. *J Appl Phys*. 993;73(1):6304–6. DOI: 10.1063/1.352678.
45. Cheng Z, Yang H. Synthesis and magnetic properties of Sm–$Y_3Fe_5O_{12}$ nanoparticles. *Physica E*. 2007;39:198–202. DOI: 10.1016/j.physe.2007.04.003.
46. Kniga MV, Rubinchik YaS, Kuligina MP. Kinetics of reaction in the Sm_2O_3-Fe_2O_3 system. *Izv AN BSSR Ser Khim Nauk*. 1969;3:30–3.
47. Katsura T, Kitayama K, Sugihara T, Kimizuka N. Thermochemical properties of Lanthanoid-Iron-Perovskite at high temperatures. *Bull Chem Soc Jpn*. 1975;48(6):1809–11.
48. Katsura T, Sekine T, Kitayama K, Sugihara T. Thermodynamic properties of Fe-Lanthanoid-O compounds at high temperatures. *J Solid State Chem*. 1978;23:43–57. DOI: 10.1016/0022-4596(78)90052-X.
49. Kimizuka N, Yamamoto A, Ohashi H, Sugihara T, Sekine T. The stability of the phases in the Ln_2O_3-FeO-Fe_2O_3 systems which are stable at elevated temperatures (Ln: lanthanide elements and Y). *J Solid State Chem*. 1983;49:65–76. DOI: 10.1016/0022-4596(83)90217-7.
50. Istomin SYa, Drozhzhin OA, Svensson G, Antipov EV. Synthesis and characterization of $Sr_{1-x}Ln_xCoO_{3-\delta}$, Ln = Y, Sm–Tm, $0.1 \le x \le 0.5$. *Solid State Scien*. 2004;6:539–46. DOI: 10.1016/j.solidstatesciences.2004.03.029.
51. Kovalevsky AV, Kharton VV, Tikhonovich VN, Naumovich EN, Tonoyan AA, Reut OP, Boginsky LS. Oxygen permeation through $Sr(Ln)CoO_{3-d}$ (Ln=La, Nd, Sm, Gd) ceramic membranes. *Mater Sci Eng B*. 1998; B52:105–16. DOI: 10.1016/S0921-5107(97)00292-4.
52. Jung KH, Choi S-M, Park H-H, Seo W-S. High temperature thermoelectric properties of Sr and Fe doped $SmCoO_3$ perovskite structure. *Current Applied Physics*. 2011;11: S260–5. DOI: 10.1016/j.cap.2010.12.032.
53. Kang JW, Ryu KH, Yo CH. Studies of nonstoichiometry and physical properties of the perovskite $Sm_{1-x}Sr_xCoO_{3-y}$ system. *Bull Korean Chem Soc*. 1995;16(7):600–3.
54. James M, Cassidy D, Glossens DJ, Withers RL. The phase diagram and tetragonal superstructures of the rare earth cobaltate phases $Ln_{1-x}Sr_xCoO_{3-\delta}$ (Ln = La^{3+}, Pr^{3+}, Nd^{3+}, Sm^{3+}, Gd^{3+}, Y^{3+}, Ho^{3+}, Dy^{3+}, Er^{3+}, Tm^{3+} and Yb^{3+}). *J Solid State Chem*. 2004;177:1886–95. DOI: 10.1016/j.jssc.2004.01.012
55. James M, Cassidy D, Wilson KF, Horvat J, Withers RL. Oxygen vacancy ordering and magnetism in the rare earth stabilized perovskite form of "$SrCoO_{3-\delta}$". *Solid State Scien*. 2004;6:655–62. DOI: 10.1016/j.solidstatesciences.2003.03.001.
56. Baek SW, Kim JH, Bae J. Characteristics of ABO_3 and A_2BO_4 (A = Sm, Sr; B = Co, Fe, Ni) samarium oxide system as cathode material for intermediate temperature-operating solid oxide fuel cell. *Solid State Ionics*. 2008;179:1570–4. DOI: 10.1016/j.ssi.2007.12.010.

57. Yang S, He T, He Q. $Sm_{0.5}Sr_{0.5}CoO_3$ cathode material from glycine-nitrate process: Formation, characterization, and application in $LaGaO_3$-based solid oxide fuel cells. *J Alloys Compd*. 2008;450:400–4. DOI: 10.1016/j.jallcom.2006.10.147.
58. Dong F, Chen D, Ran R, Park H, Kwak C, Shao Z. A comparative study of $Sm_{0.5}Sr_{0.5}MO_{3-d}$ (M = Co and Mn) as oxygen reduction electrodes for solid oxide fuel cells. *Int J Hydrogen Energy*. 2012; 37:4377–87. DOI: 10.1016/j.ijhydene.2011.11.150.
59. Volkova NE, Maklakova AV, Gavrilova LYa, Cherepanov VA. Phase equilibria, crystal structure and properties of intermediate oxides in the Sm_2O_3 – SrO – CoO system. *Eur J Inorg Chem*. 2017;2017(26):3285–92. DOI: 10.1002/ejic.201700321.
60. Cherepanov VA, Barkhatova LYu, Petrov AN, Voronin VI. Phase equilibria in the La-Sr-Co-O system and thermodynamic stability of the single phases. Solid Oxide Fuel Cells IV. M. Dokiya, O. Yamamoto, H. Tagawa, S. C. Singhal, editors. PV 95–1, p.434–443, The Electrochemical Society Proceedings Series, Pennington, NJ (1995).
61. Song HS, Min J-H, Kim J, Moon J. Phase stability of $Sm_{0.5}Sr_{0.5}CoO_3$ cathodes for on-planar type, single-chamber, solid oxide fuel cells. *J Power Sources*. 2009;191:269–74. DOI: 10.1016/j.jpowsour.2009.02.028.
62. Wang Y, Nie H, Wang S, Wen T-L, Guth U, Valshook V. $A_{2-\alpha}A'_{\alpha}BO_4$-type oxides as cathode materials for IT-SOFCs (A = Pr, Sm; A' = Sr; B = Fe, Co). *Mater Lett*. 2006;60:1174–8. DOI: 10.1016/j.matlet.2005.10.104.
63. James M, Tedesco A, Cassidy D, Colella M, Smythe PJ. The phase diagram and crystal chemistry of strontium-doped rare earth cobaltates: $Ln_{2-x}Sr_xCoO_{4+\delta}$ (Ln = La–Dy). *J Alloy Compd.* 2006;419:201–7. DOI: 10.1016/j.jallcom.2005.08.080.
64. Siwen L, Yufang R. The synthesis and physical properties of the new layered lanthanide alkaline earth cobalt oxides [$Ln_2MCo_2O_7$ (Ln = Sm, Gd; M = Sr, Ba)]. *Mater Res Bull.* 1994;29:993–1000. DOI: 10.1016/0025–5408(94)90061–2.
65. Park SK, Ishikawa T, Tokura Y, Li JQ, Matsui Y. Variation of charge-ordering in $R_{1/3}Sr_{2/3}FeO_3$ (R=La, Pr, Nd, Sm, and Gd). *Phys Rev B*. 1999;60:10788–95. DOI: 10.1103/PhysRevB.60.10788.
66. Zhao YM, Hervieu M, Nguyen N, Raveau B. Charge Ordering and Magnetotransport Transitions in $Sm_{1/3}Sr_{2/3}FeO_{3-\delta}$. *J Solid State Chem.* 2000;153:140–4. DOI: 10.1006/jssc.2000.8763.
67. Lu X, Chen Y, Ding Y, Lin B. A cobalt-free $Sm_{0.5}Sr_{0.5}FeO_3{}^{-}{}_{\delta}$ – $BaZr_{0.1}Ce_{0.7}Y_{0.2}O_{3-\delta}$ composite cathode for proton-conducting solid oxide fuel cells. *Int J Hydrogen Energy*. 2012;37:8630–4. DOI: 10.1016/j.ijhydene.2012.02.050.
68. Anderson MD, Stevenson JW, Simner SP. Reactivity of lanthanide ferrite SOFC cathodes with YSZ electrolyte. *J Power Sources*. 2004;129:188–92. DOI: 10.1016/j.jpowsour.2003.11.039.
69. Ren Y, Küngas R, Gorte RJ, Deng C. The effect of A-site cation (Ln=La, Pr, Sm) on the crystal structure, conductivity and oxygen reduction properties of Sr-doped ferrite perovskites. *Solid State Ionics.* 2012;212:47–54. DOI: 10.1016/j.ssi.2007.12.010.
70. Kharton VV, Kovalevsky AV, Patrakeev MV, Tsipis EV, Viskup AP, Kolotygin VA, Yaremchenko AA, Shaula AL, Kiselev EA, Waerenborgh JC. Oxygen Nonstoichiometry, Mixed Conductivity, and Mössbauer Spectra of $Ln_{0.5}A_{0.5}FeO_{3-\delta}$

(Ln = La-Sm, A = Sr, Ba): Effects of Cation Size. *Chem Mater*. 2008;20:6457–67. DOI: 10.1021/cm801569j.
71. Khvostova LV, Volkova NE, Gavrilova LYa, Cherepanov VA. Crystal structure, oxygen nonstoichiometry and properties of novel Ruddlesden-Popper phase $Sm_{1.8}Sr_{1.2}Fe_2O_{7-\delta}$. *Mater Lett*. 2018;213:158–61. DOI: 10.1016/j.matlet.2017.11.041.
72. Gavrilova LYa, Aksenova TV, Volkova NE, Podzorova AS, Cherepanov VA. Phase equilibria and crystal structure of the complex oxides in the Ln–Ba–Co–O (Ln=Nd, Sm) systems. *J Solid State Chem.* 2011;184:2083–7. DOI: 10.1016/j.jssc.2011.06.006.
73. Khalyavin DD, Sazonov AP, Troyanchuk IO, Szymczak R, Szymczak H. Phase relations in the systems $Ln_{1-x}Ba_xCoO_{3-\delta}$ ($0 < x \leq 0.66$; Ln = Nd, Sm). *Inorg Mater.* 2003;39:1092–6. DOI: 10.1023/A:10260556.
74. Maignan A, Martin C, Pelloquin D, Nguyen N, Raveau B. Structural and Magnetic Studies of Ordered Oxygen-Deficient Perovskites $LnBaCo_2O_{5+\delta}$, Closely Related to the "112" Structure. *J Solid State Chem.* 1999;142:247–60. DOI: 10.1006/jssc.1998.7934.
75. Millange F, Caignaert V, Domengès B, Raveau B. Order-Disorder Phenomena in New $LaBaMn_2O_{6-x}$ CMR Perovskites. Crystal and Magnetic Structure. *Chem Mater.* 1998;10:1974–83. DOI: 10.1021/cm980130v
76. Zhou W, Lin CT, Liang WY. Synthesis and Structural Studies of the Perovskite-Related Compound $YBaCo_2O_{5+x}$. *Adv Mater*. 1993; 5(10)735–8. DOI: 10.1002/adma.19930051010.
77. Tsvetkov DS, Sereda VV, Zuev AYu. Oxygen nonstoichiometry and defect structure of the double perovskite $GdBaCo_2O_{6-\delta}$. *Solid State Ionics*. 2010;180:1620–5. DOI: 10.1016/j.ssi.2009.10.014.
78. Anderson PS, Kirk CA, Knudsen J, Reaney IM, West AR. Structural characterization of $ReBaCo_2O_{6-\delta}$ phases (RE = Pr, Nd, Sm, Eu, Gd, Tb, Dy, Ho). *Solid State Scien*. 2005;7:1149–56. DOI: 10.1016/j.solidstatesciences.2005.03.004.
79. Seikh MdM, Simon Ch, Caignaert V, Pralong V, Lepetit MB, Boudin S, Raveau B. New Magnetic Transitions in the Ordered Oxygen-Deficient Perovskite $LnBaCo_2O_{5.50+\delta}$. *Chem Mater*. 2008;20:231–8. DOI: 10.1021/cm7026652.
80. Kim J-H, Kim Y, Connor PA, Irvine J, Bae J, Zhou W. Structural, thermal and electrochemical properties of layered perovskite $SmBaCo_2O_{5+d}$, a potential cathode material for intermediate-temperature solid oxide fuel cells. *J Power Sources*. 2009;194:704–11. DOI: 10.1016/j.jpowsour.2009.06.024.
81. Aksenova TV, Gavrilova LYu, Yaremchenko AA, Cherepanov VA, Kharton VV. Oxygen nonstoichiometry, thermal expansion and high-temperature electrical properties of layered $NdBaCo_2O_{5+\delta}$ and $SmBaCo_2O_{5+\delta}$. *Mat Res Bull*. 2010;45:1288–92. DOI: 10.1016/j.materresbull.2010.05.004.
82. Sun W, Bi L, Yan L, Peng R, LiuW. Synthesis of $SmBaCo_2O_{6-\delta}$ powder by the combustion process using Co_3O_4 as precursor. *J Alloys Compd*. 2009;481: L40–2. DOI: 10.1016/j.jallcom.2009.03.150.
83. Zhang K, Ge L, Ran R, Shao Z, Lio S. Synthesis, Characterization and Evaluation of Cation-Ordered $LnBaCo_2O_{5+\delta}$ as Materials of Oxygen Permeation Membranes and Cathodes of SOFCs. *Acta Mater*. 2008;56:4876–89. DOI: 10.1016/j.actamat.2008.06.004.

84. Volkova NE, Gavrilova LYa, Cherepanov VA, Aksenova TV, Kolotygin VA, Kharton VV. Synthesis, crystal structure and properties of $SmBaCo_{2-x}Fe_xO_{5+\delta}$. *J Solid State Chem.* 2013;204:219–23. DOI: 10.1016/j.jssc.2013.06.001.
85. Lomakov MV, Istomin SYa, Abakumov AM, Van Tandeloo G, Antipov EV. Synthesis and characterization of oxygen-deficient oxides $BaCo_{1-x}Y_xO_{3-y}$, x=0.15, 0.25 and 0.33, with the perovskite structure. *Solid State Ionics.* 2008;179:1885–9. DOI: 10.1016/j.ssi.2008.05.004.
86. Siwen L, Yufang R. Studies on the synthetic, structural, electrical, and magnetic properties of the new layered oxides $Ln_2MCo_2O_7$ (Ln = Sm, Gd; M = Sr, Ba). *J Solid State Chem*. 1995;114:286–8. DOI: 10.1006/jssc.1995.1042.
87. Gillie LJ, Hadermann J, Hervieu M, Maignan A, Martin C. Oxygen Vacancy Ordering in the Double-layered Ruddlesden-Popper Cobaltite $Sm_2BaCo_2O_{7-\delta}$. *Chem Mater*. 2008;20:6231–7. DOI: 10.1021/cm8010138.
88. Zhiyu Q, Xianran X, Wenxia Y, Soukun W, Xiaolong C, Jingkui L, Sishen X. Phase relations and compounds in the Sm_2O_3 – BaO – CuO system at 950 °C in air. *J Alloys Compd.* 1993;202:77–80. DOI: 10.1016/0925-8388(93)90521-N.
89. Subasri R, Sreedharan OM. Thermodynaqmic stabilities of Ln_2BaO_4 (Ln = Nd, Sm, Eu or Gd) by CaF_2 – based Emf measurements. *J Alloys Compd*. 1998;274:153–6. DOI: 10.1016/S0925-8388(98)00548-9.
90. Karen P, Woodward PM, Santhosh PN, Vogt T, Stephens PW, Pagola SJ. Verwey transition under oxygen loading in $RBaFe_2O_{5+w}$ (R=Nd and Sm). *J Solid State Chem.* 2002;167:480–93. DOI: 10.1006/jssc.2002.9665.
91. Karen P, Woodward PM. Synthesis and structural investigations of the double perovskites $REBaFe_2O_{5+w}$ (RE=Nd, Sm). *J Mater Chem.* 1999;9:789–97. DOI: 10.1039/A809302D.
92. Moritomo Y, Hanawa M, Ohishi Y, Kato K, Nakamura J, Karppinen M, Yamauchi H. Physical pressure effect on the charge-ordering transition of $BaSmFe_2O_{5.0}$. *Phys Rev B*. 2003;68:060101(4). DOI: 10.1103/PhysRevB.68.060101.
93. Elzubair A, El Massalami M, Domingues PH. On the structure and magnetic properties of the series $RBa_2Fe_3O_{8+x}$ (R = La, Nd, Sm, Gd). *Physica B.* 1999;271:284–93. DOI: 10.1016/S0921-4526(99)00205-7.
94. Lindén J, Karen P, Kjekshus A, Miettinen J, Karppinen M. Partial oxygen ordering in cubic perovskite $REBa_2Fe_3O_{8+w}$ (RE = Gd, Eu, Sm, Nd). *J Solid State Chem*. 1999;144:398–404. DOI: 10.1006/jssc.1999.8178.
95. Volkova NE, Lebedev OI, Gavrilova LYa, Turner S, Gauquelin N, Seikh MdM, Caignaert V, Cherepanov VA, Raveau B, van Tendeloo G. Nanoscale Ordering in Oxygen Deficient Quintuple Perovskite $Sm_{2-\varepsilon}Ba_{3+\varepsilon}Fe_5O_{15-\delta}$: Implication for Magnetism and Oxygen Stoichiometry. *Chem Mater*. 2014;26:6303–10. DOI: 10.1021/cm503276p.
96. Volkova NE, Urusova AS, Gavrilova LYa, Bryuzgina AV, Deryabina KM, Mychinko MYu, Lebedev OI, Raveau B, Cherepanov VA. Special Features of Phase Equilibriums in Ln–Ba–Fe–O Systems. *Russian Journal of General Chemistry.* 2016;86(8):1800–4. DOI: 10.1134/S1070363216080041.

97. Itagaki Y, Mori M, Hosoya Y, Aono H, Sadaoka Y. O_3 and NO_2 sensing properties of $SmFe_{1-x}Co_xO_3$ perovskite oxides. *Sens Actuators, B.* 2007;122:315–20. DOI: 10.1016/j.snb.2006.06.001.
98. Zhao M, Peng H, Hu J, Han Z. Effect of Cobalt doping on the microstructure, electrical and ethanol-sensing properties of $SmFe_{1-x}Co_xO_3$. *Sens Actuators, B.* 2008;129:953–7. DOI: 10.1016/j.snb.2007.10.012.
99. Mori M, Itagaki Y, Sadaoka Y. Effect of VOC on ozone detection using semiconducting sensor with $SmFe_{1-x}Co_xO_3$ perovskite-type oxide. *Sens Actuators, B.* 2012;163:44–50. DOI: 10.1016/j.snb.2011.12.047.
100. Zhao M, Peng H, Fang S, Hu J. Microstructure, electrical and ethanol-sensing properties of perovskite-type $SmFe_{0.7}Co_{0.3}O_3$. *Sens Actuators, B.* 2008;130:609–13. DOI: 10.1016/j.snb.2007.10.017.
101. Zhang R, Hu J, Zhao M, Han Z, Wei J, Wu Z, Qin H, Wang K. Elecctrical and CO-sensing properties of $SmFe_{0.7}Co_{0.3}O_3$ perovskite oxide. *Mater Sci Eng, B.* 2010;171:139–43. DOI: 10.1016/j.mseb.2010.03.087.
102. Galayda AP, Volkova NE, Gavrilova LYa, Balymov KG, Cherepanov VA. Phase equilibria, structure and properties of intermediate phases in the Sm_2O_3 – Fe_2O_3 – CoO and Sm_2O_3 – CaO – CoO systems. *J Alloys Compd.* 2017;718:288–97. DOI: 10.1016/j.jallcom.2017.05.044.
103. Ben Tahar L, Smiri LS, Artus M, Joudrier A-L, Herbst F, Vaulay MJ, Ammar S, Fiévet F. Characterization and magnetic properties of Sm- and Gd-substituted $CoFe_2O_4$ nanoparticles prepared by forced hydrolysis in polyol. *Mater Res Bull.* 2007;42:1888–96. DOI: 10.1016/j.materresbull.2006.12.014.
104. Ben Tahar L, Artus M, Ammar S, Smiri LS, Herbst F, Vaulay M-J, Richard V, Grenèche J-M, Villain F, Fiévet F. Magnetic properties of $CoFe_{1.9}RE_{0.1}O_4$ nanoparticles (RE = La, Ce, Nd, Sm, Eu, Gd, Tb, Ho) prepared in polyol. *J Magn Magn Mater.* 2008;320:3242–50. DOI: 10.1016/j.jmmm.2008.06.031.
105. Guo L, Shen X, Song F, Lin L, Zhu Y. Structure and magnetic properties of $CoFe_{2-x}Sm_xO_4$ (x = 0–0.2) nanofibers prepared by sol-gel route. *Mater Chem Phys.* 2011;129:943–7. DOI: 10.1016/j.matchemphys.2011.05.023.
106. Ruiz MM, Mietta JL, Antonel PS, Pérez OE, Negri RM, Jorge G. Structural and magnetic properties of $Fe_{2-x}CoSm_xO_4$-nanoparticles and $Fe_{2-x}CoSm_xO_4$-PDMS magnetoelastomers as a function of Sm content. *J Magn Magn Mater.* 2013;327:11–9. DOI: 10.1016/j.jmmm.2012.09.020.
107. Rashad MM, Mohamed RM, El-Shall H. Magnetic properties of nanocrystalline Sm-substituted $CoFe_2O_4$ synthesized by citrate precursor method. *J Mater Process Technol.* 2008;198:139–46. DOI: 10.1016/j.jmatprotec.2007.07.012.
108. Alifanti M, Bueno G, Parvulescu V, Parvulescu VI, Corberán VC. Oxidation of ethane on high specific surface $SmCoO_3$ and $PrCoO_3$ perovskites. *Catal Today.* 2009;143:309–14. DOI: 10.1016/j.cattod.2009.02.026.